Research Article | Vol. 7, No. 9 | 1 Sep 2016 | BIOMEDICAL OPTICS EXPRESS 3377

Biomedical Optics EXPRESS

Imaging hemodynamic response after ischemic stroke in mouse cortex using visible-light optical coherence tomography

SIYU CHEN,[1,3] QI LIU,[1,2,3] XIAO SHU,[1] BRIAN SOETIKNO,[1] SHANBAO TONG,[2] AND HAO F. ZHANG[1,*]

[1]*Department of Biomedical Engineering, Northwestern University, Evanston, IL 60208, USA*
[2]*School of Biomedical Engineering, Shanghai Jiao Tong University, Shanghai, China*
[3]*Both authors contributed equally to this work*
[*]*hfzhang@northwestern.edu*

Abstract: Visible-light optical coherence tomography (Vis-OCT) is an emerging technology that can image hemodynamic response in microvasculature. Vis-OCT can retrieve blood oxygen saturation (sO_2) mapping using intrinsic optical absorption contrast while providing high-resolution anatomical vascular structures at the same time. To improve the accuracy of Vis-OCT oximetry on vessels embedded in highly scattering medium, i.e., brain cortex, we developed and formulated a novel dual-depth sampling and normalization strategy that allowed us to minimize the detrimental effect of ubiquitous tissue scattering. We applied our newly developed approach to monitor the hemodynamic response in mouse cortex after focal photothrombosis. We observed vessel dilatation, which was negatively correlated with the original vessel diameter, in the penumbra region. The sO_2 of vessels in the penumbra region also dropped below normal range after focal ischemia.

OCIS codes: (110.4500) Optical coherence tomography; (170.1460) Blood gas monitoring; (170.2655) Functional monitoring and imaging; (170.6480) Spectroscopy, speckle.

References and links

1. S. P. Chong, C. W. Merkle, C. Leahy, and V. J. Srinivasan, "Cerebral metabolic rate of oxygen ($CMRO_2$) assessed by combined Doppler and spectroscopic OCT," Biomed. Opt. Express **6**(10), 3941–3951 (2015).
2. R. K. Wang, S. L. Jacques, Z. Ma, S. Hurst, S. R. Hanson, and A. Gruber, "Three dimensional optical angiography," Opt. Express **15**(7), 4083–4097 (2007).
3. U. Dirnagl, C. Iadecola, and M. A. Moskowitz, "Pathobiology of ischaemic stroke: an integrated view," Trends Neurosci. **22**(9), 391–397 (1999).
4. K. P. Doyle, R. P. Simon, and M. P. Stenzel-Poore, "Mechanisms of ischemic brain damage," Neuropharmacology **55**(3), 310–318 (2008).
5. B. C. White, J. M. Sullivan, D. J. DeGracia, B. J. O'Neil, R. W. Neumar, L. I. Grossman, J. A. Rafols, and G. S. Krause, "Brain ischemia and reperfusion: molecular mechanisms of neuronal injury," J. Neurol. Sci. **179**(1-2 S 1-2), 1–33 (2000).
6. L. Hertz, "Bioenergetics of cerebral ischemia: a cellular perspective," Neuropharmacology **55**(3), 289–309 (2008).
7. M. A. Moskowitz, E. H. Lo, and C. Iadecola, "The science of stroke: mechanisms in search of treatments," Neuron **67**(2), 181–198 (2010).
8. R. D. Frostig, E. E. Lieke, D. Y. Ts'o, and A. Grinvald, "Cortical functional architecture and local coupling between neuronal activity and the microcirculation revealed by in vivo high-resolution optical imaging of intrinsic signals," Proc. Natl. Acad. Sci. U.S.A. **87**(16), 6082–6086 (1990).
9. A. K. Dunn, H. Bolay, M. A. Moskowitz, and D. A. Boas, "Dynamic imaging of cerebral blood flow using laser speckle," J. Cereb. Blood Flow Metab. **21**(3), 195–201 (2001).
10. S. Hu, K. Maslov, V. Tsytsarev, and L. V. Wang, "Functional transcranial brain imaging by optical-resolution photoacoustic microscopy," J. Biomed. Opt. **14**(4), 040503 (2009).
11. M. B. Bouchard, V. Voleti, C. S. Mendes, C. Lacefield, W. B. Grueber, R. S. Mann, R. M. Bruno, and E. M. C. Hillman, "Swept confocally-aligned planar excitation (SCAPE) microscopy for high speed volumetric imaging of behaving organisms," Nat. Photonics **9**(2), 113–119 (2015).
12. M. A. Yaseen, V. J. Srinivasan, I. Gorczynska, J. G. Fujimoto, D. A. Boas, and S. Sakadžić, "Multimodal optical imaging system for in vivo investigation of cerebral oxygen delivery and energy metabolism," Biomed. Opt. Express **6**(12), 4994–5007 (2015).

#266912 http://dx.doi.org/10.1364/BOE.7.003377
Journal © 2016 Received 24 May 2016; revised 23 Jul 2016; accepted 3 Aug 2016; published 10 Aug 2016

Biomedical Optics EXPRESS

13. A. Y. Shih, J. D. Driscoll, P. J. Drew, N. Nishimura, C. B. Schaffer, and D. Kleinfeld, "Two-photon microscopy as a tool to study blood flow and neurovascular coupling in the rodent brain," J. Cereb. Blood Flow Metab. **32**(7), 1277–1309 (2012).
14. S. Sakadžić, J. Lee, D. A. Boas, and C. Ayata, "High-resolution in vivo optical imaging of stroke injury and repair," Brain Res. **1623**, 174–192 (2015).
15. S. Sakadzić, E. Roussakis, M. A. Yaseen, E. T. Mandeville, V. J. Srinivasan, K. Arai, S. Ruvinskaya, A. Devor, E. H. Lo, S. A. Vinogradov, and D. A. Boas, "Two-photon high-resolution measurement of partial pressure of oxygen in cerebral vasculature and tissue," Nat. Methods **7**(9), 755–759 (2010).
16. U. Dirnagl, B. Kaplan, M. Jacewicz, and W. Pulsinelli, "Continuous measurement of cerebral cortical blood flow by laser-Doppler flowmetry in a rat stroke model," J. Cereb. Blood Flow Metab. **9**(5), 589–596 (1989).
17. V. J. Srinivasan, J. Y. Jiang, M. A. Yaseen, H. Radhakrishnan, W. Wu, S. Barry, A. E. Cable, and D. A. Boas, "Rapid volumetric angiography of cortical microvasculature with optical coherence tomography," Opt. Lett. **35**(1), 43–45 (2010).
18. R. U. Maheswari, H. Takaoka, H. Kadono, R. Homma, and M. Tanifuji, "Novel functional imaging technique from brain surface with optical coherence tomography enabling visualization of depth resolved functional structure in vivo," J. Neurosci. Methods **124**(1), 83–92 (2003).
19. Y. Chen, A. D. Aguirre, L. Ruvinskaya, A. Devor, D. A. Boas, and J. G. Fujimoto, "Optical coherence tomography (OCT) reveals depth-resolved dynamics during functional brain activation," J. Neurosci. Methods **178**(1), 162–173 (2009).
20. F. E. Robles, S. Chowdhury, and A. Wax, "Assessing hemoglobin concentration using spectroscopic optical coherence tomography for feasibility of tissue diagnostics," Biomed. Opt. Express **1**(1), 310–317 (2010).
21. J. Yi and X. Li, "Estimation of oxygen saturation from erythrocytes by high-resolution spectroscopic optical coherence tomography," Opt. Lett. **35**(12), 2094–2096 (2010).
22. S. P. Chong, C. W. Merkle, C. Leahy, H. Radhakrishnan, and V. J. Srinivasan, "Quantitative microvascular hemoglobin mapping using visible light spectroscopic Optical Coherence Tomography," Biomed. Opt. Express **6**(4), 1429–1450 (2015).
23. J. Yi, Q. Wei, W. Liu, V. Backman, and H. F. Zhang, "Visible-light optical coherence tomography for retinal oximetry," Opt. Lett. **38**(11), 1796–1798 (2013).
24. B. D. Watson, W. D. Dietrich, R. Busto, M. S. Wachtel, and M. D. Ginsberg, "Induction of reproducible brain infarction by photochemically initiated thrombosis," Ann. Neurol. **17**(5), 497–504 (1985).
25. M. Schroeter, S. Jander, and G. Stoll, "Non-invasive induction of focal cerebral ischemia in mice by photothrombosis of cortical microvessels: characterization of inflammatory responses," J. Neurosci. Methods **117**(1), 43–49 (2002).
26. M. D. Ginsberg and R. Busto, "Rodent models of cerebral ischemia," Stroke **20**(12), 1627–1642 (1989).
27. J. Yi, S. Chen, V. Backman, and H. F. Zhang, "In vivo functional microangiography by visible-light optical coherence tomography," Biomed. Opt. Express **5**(10), 3603–3612 (2014).
28. N. Lue, J. Bewersdorf, M. D. Lessard, K. Badizadegan, R. R. Dasari, M. S. Feld, and G. Popescu, "Tissue refractometry using Hilbert phase microscopy," Opt. Lett. **32**(24), 3522–3524 (2007).
29. M. Wojtkowski, R. Leitgeb, A. Kowalczyk, T. Bajraszewski, and A. F. Fercher, "In vivo human retinal imaging by Fourier domain optical coherence tomography," J. Biomed. Opt. **7**(3), 457–463 (2002).
30. A. F. Fercher, W. Drexler, C. K. Hitzenberger, and T. Lasser, "Optical coherence tomography - principles and applications," Rep. Prog. Phys. **66**(2), 239–303 (2003).
31. M. Wojtkowski, V. Srinivasan, T. Ko, J. Fujimoto, A. Kowalczyk, and J. Duker, "Ultrahigh-resolution, high-speed, Fourier domain optical coherence tomography and methods for dispersion compensation," Opt. Express **12**(11), 2404–2422 (2004).
32. M. Guizar-Sicairos, S. T. Thurman, and J. R. Fienup, "Efficient subpixel image registration algorithms," Opt. Lett. **33**(2), 156–158 (2008).
33. J. Lee, V. Srinivasan, H. Radhakrishnan, and D. A. Boas, "Motion correction for phase-resolved dynamic optical coherence tomography imaging of rodent cerebral cortex," Opt. Express **19**(22), 21258–21270 (2011).
34. S. Sakadžić, E. T. Mandeville, L. Gagnon, J. J. Musacchia, M. A. Yaseen, M. A. Yucel, J. Lefebvre, F. Lesage, A. M. Dale, K. Eikermann-Haerter, C. Ayata, V. J. Srinivasan, E. H. Lo, A. Devor, and D. A. Boas, "Large arteriolar component of oxygen delivery implies a safe margin of oxygen supply to cerebral tissue," Nat. Commun. **5**, 5734 (2014).
35. N. Bosschaart, G. J. Edelman, M. C. G. Aalders, T. G. van Leeuwen, and D. J. Faber, "A literature review and novel theoretical approach on the optical properties of whole blood," Lasers Med. Sci. **29**(2), 453–479 (2014).
36. A. Y. Shih, B. Friedman, P. J. Drew, P. S. Tsai, P. D. Lyden, and D. Kleinfeld, "Active dilation of penetrating arterioles restores red blood cell flux to penumbral neocortex after focal stroke," J. Cereb. Blood Flow Metab. **29**(4), 738–751 (2009).
37. M. Ishikawa, E. Sekizuka, C. Oshio, S. Sato, N. Yamaguchi, S. Terao, K. Tsukada, H. Minamitani, and T. Kawase, "Platelet adhesion and arteriolar dilation in the photothrombosis: observation with the rat closed cranial and spinal windows," J. Neurol. Sci. **194**(1), 59–69 (2002).
38. A. G. Tsai, P. C. Johnson, and M. Intaglietta, "Oxygen gradients in the microcirculation," Physiol. Rev. **83**(3), 933–963 (2003).
39. P. Moftakhar, J. S. Hauptman, D. Malkasian, and N. A. Martin, "Cerebral arteriovenous malformations. Part 2: physiology," Neurosurg. Focus **26**(5), E11 (2009).

Biomedical Optics EXPRESS

40. K. Masamoto, N. Takizawa, H. Kobayashi, K. Oka, and K. Tanishita, "Dual responses of tissue partial pressure of oxygen after functional stimulation in rat somatosensory cortex," Brain Res. **979**(1-2), 104–113 (2003).
41. C. D. Klaassen, "Pharmacokinetics of rose bengal in the rat, rabbit, dog and guinea pig," Toxicol. Appl. Pharmacol. **38**(1), 85–100 (1976).

1. Introduction

Continuous cerebral circulation and sufficient oxygen supply are critical for maintaining the normal functionality of the brain [1]. During ischemic stroke (IS), impairments of the vascular network restrict the ability of brain to regulate blood supply [2]. Reduced cerebral blood flow (CBF) results in a shortage of oxygen delivery and the accumulation of toxic metabolic wastes, causing irreversible brain injury [3].

The underlying mechanisms of neuronal death in IS depend on several factors, including the severity of the ischemia, the location of neurons, and the time course along IS onset. For example, in the ischemic core, where the blood supply relies solely on the occluded vessel, excitotoxicity and acidotoxicity contribute to acute neuron necrosis. In contrast, in the penumbra region, where collateral blood flow can maintain certain cell functions, delayed neuron death may be caused by peri-infarct depolarization, oxidative and nitrative stress, inflammation, and apoptosis [3–5].

The activation of these stroke pathophysiological pathways is often associated with changes in the cerebral oxygen metabolism ($CMRO_2$). Alterations in $CMRO_2$ and neuron survivability are hypothesized to be closely related [6,7]. Fundamental studies on such connections will shed light on how they affect and determine the destiny of neurons. Such discoveries can help to evaluate the effectiveness of treatments in terms of regulating neuron metabolism and preventing cell death, eventually benefiting IS patients.

Current techniques for monitoring $CMRO_2$ can be classified into three main categories: (1) functional magnetic resonance imaging (fMRI), (2) positron emission tomography (PET), and (3) functional optical imaging. fMRI and PET are well-established methods in functional brain imaging and the only ones that are clinically available; however, both fMRI and PET have low spatial (~1 mm) and temporal resolution, and the need for radioactive tracers further impedes the applications of PET.

Functional optical imaging is a collection of emerging research tools for brain hemodynamics [8–12]. Among these tools, two-photon (TP) and multi-photon (MP) fluorescence microscopy have been commonly adopted in neuroscience studies due to their enhanced imaging depth into the cortex (> 1mm) [13,14]. Using oxygen-sensitive florescent dye, TP and MP fluorescence microscopy can provide three-dimensional (3D) oxygen mapping at micrometer-scale resolution [15]. When combined with optical blood flow measurements, regional oxygen consumption can be obtained [9,16]; however, the required extrinsic contrast agents increase the complexity of the experiment and may introduce additional confounding factors.

Meanwhile, label-free optical determination of blood oxygenation is achievable thanks to the contrasting optical absorption spectra of oxy- and deoxy-hemoglobin. Using two or more imaging wavelengths, optical intrinsic signal (OIS) imaging and laser speckle imaging (LSI) can yield information about changes in blood oxygenation and blood flow; however, both OIS and LSI lack depth resolution and can only be applied to superficial vessels [13]. Functional photoacoustic (PA) microscopy, on the other hand, can generate 3D tomography of cortical vascular structure based solely on absorption contrast. High-definition cortical vascular network and blood oxygen saturation (sO_2) maps acquired by PA microscopy have been reported [10], yet the required mechanical coupling between the target tissue and the ultrasonic transducer poses a major challenge: such coupling cannot be guaranteed if the cranial window is sealed for long-term monitoring or if a large field-of-view is desirable.

Function optical coherence tomography (OCT) recently has emerged as a potential candidate for $CMRO_2$ monitoring. OCT is a low-coherence interferometry-based imaging technique that can resolve high-definition 3D structural information *in vivo*. Recent advances

Biomedical Optics EXPRESS

in OCT technology have enabled hemodynamic measurements. Notably, multiple groups have explored cortical vascular networks and cerebral circulation using OCT angiography (OCTA) [17–19]. In addition, spectroscopic OCT is intrinsically sensitive to the oxygen saturation (sO_2)-dependent hemoglobin absorption, especially when broadband visible light illumination is used [20,21]. Attempts to quantify blood sO_2 in major cortical vessels have been reported [22].

In all previous OCT and OCTA oximetry attempts, tissue scattering was either compensated for numerically or ignored completely [22,23]; however, these approaches are inadequate when dealing with cortical tissues, which are highly optical scattering. Here, we propose a new sampling and normalization strategy which incorporates taking the spectroscopic OCTA measurement at two different depth planes to minimize the adverse influences from strong wavelength-dependent tissue scattering. The corresponding theoretical formation and its implications were developed and discussed.

In this study we monitored the hemodynamic changes on mouse cortex following acute photothrombosis *in vivo* using visible-light OCT (Vis-OCT). The photothrombosis model was a focal ischemic stroke model, which is favored by many researchers because the infarct size and location can be easily controlled [24,25]. Photothrombosis was induced by a photochemical reaction, which was activated by the illumination of intravenously injected Rose Bengal dye. The reaction generated free oxygen radicals, disturbed endothelial function, and resulted in thrombosis formation [26]. By comparing Vis-OCT measurements before and after photothrombosis, we were able to characterize the hemodynamic changes of photothrombotic stroke in mouse.

2. Methods and materials

2.1 System design

We adopted our previously reported spectral-domain Vis-OCT to image the mouse brain *in vivo* [27]. Figure 1(a) illustrates the schematic diagram of the experimental setup. The OCT core is a free-space Michelson interferometer which incorporates a 50:50 non-polarizing beam splitter (CM1-BS013, Thorlabs, Inc.). A filtered supercontinuum source (SuperK EXTREME EXW-6 in conjunction with SPLIT VIS/IR, NKT Photonics A/S) provides broadband visible-light illumination. A pair of galvanometer mirrors (QS-7 XY, Nutfield Technology) steer the sampling beam before it is focused onto the cortical surface by a scan lens (LSM03-VIS, Thorlabs, Inc.). The lens has an effective focal length (EFL) of 39 mm, while the illumination beam diameter at the entrance pupil was 2.0 mm. We estimated the effective numerical aperture (NA) to be 0.03, and theoretical lateral resolution to be 11.9 μm. The total irradiation intensity on the sample was controlled at 1.0 mW, as measured by a calibrated power meter (Model 1918-R with 918-SL-OD2R detector, Newport Corporation). We carefully attenuated and dispersion-matched the reference beam to optimize the imaging quality. A home-built spectrometer digitized the interferogram. The spectrometer was calibrated to cover the spectrum range from 513 nm – 620 nm at a 0.066-nm interval; however, as the light intensity falls at the spectrum edges, the captured spectrum has a full width at half maximum (FWHM) bandwidth of 93 nm centered at 566 nm. Thus, the theoretical axial resolution is 1.6 μm in vacuum, or around 1.2 μm in mouse cortex if we assume its average refractive index to be ~1.37 [28].

Biomedical Optics EXPRESS

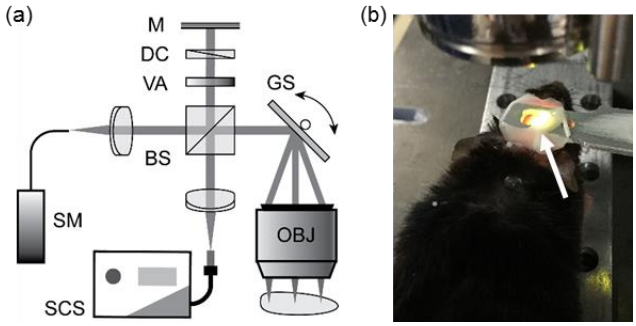

Fig. 1. (a) Schematic diagram of Vis-OCT experimental system for cortical imaging. (b) Photograph of a mouse undergoing imaging session. White arrow: homemade steel head holder to reduce motion artifacts.

2.2 Animal preparation

All experiment protocols in this study were approved by the Northwestern University Institutional Animal Care and Use Committee (IACUC). We anesthetized young adult mice (20 to 25 g) using isoflurane/air mixture (4% V/V during induction and 1.5-1.8% afterwards). During the entire procedure, we maintained the mouse core temperature at 37 °C using a homeothermic blanket system with feedback control from a temperature probe inserted into the mouse rectum (FHC, Stoelting Co.).

The mouse was secured on a stereotaxic frame for surgery. Prior to craniotomy, dexamethasone (2.0 mg/kg body weight) was injected subcutaneously to minimize cerebral edema. We carefully shaved the fur around the surgical area to expose the scalp, where lidocaine was applied topically for local anesthesia. A midline incision was made to expose soft tissues, which were then completely removed and cleaned. Then, a rectangular craniotomy window approximately 4×4 mm^2 was created using a dental drill above the right cerebral hemisphere. Meanwhile, the dura remained intact. We checked for bleeding and other signs of excessive tissue damage. If none was observed, a homemade steel head holder was gently placed around the craniotomy window and sealed using dental cement. The holder had a center window of 5×6 mm^2 for imaging, as indicated in Fig. 1(b).

After the dental cement solidified, the mouse was transferred to our animal holder for Vis-OCT imaging. The head holder was clamped to the animal holder to suppress excessive motion. A pulse oximeter was attached to the rear limb of the mouse to provide heart rate and peripheral oxygenation (spO_2) readings. We again checked for bleeding and edema within the surgical area, as well as vital signs of the mouse. If no abnormalities were found, we proceeded with Vis-OCT imaging.

We introduced focal stroke through photothrombosis in the middle of the OCT imaging process, which automatically divided the imaging process into two sessions.

To induce photothrombosis, we injected Rose Bengal dye (40 mg/mL saline solution) via the tail vein at a dosage of 133 mg/kg body weight. An unfocused 532 nm diode laser irradiated the exposed cortical area for about 30 minutes, which induced blood coagulation and vessel occlusion within the excited area. The beam diameter and energy were measured to be 2.6 mm and 30 mW, respectively. After exposure, we visually inspected the target region to ensure all major vessels were properly occluded before imaging again.

From the beginning of anesthesia to the completion of Vis-OCT imaging, the entire experiment lasted about two hours. After that, the mouse was euthanized before regaining consciousness. We performed 15 vis-OCT imaging session on different mice. Among them, five underwent photothrombosis procedure.

Biomedical Optics EXPRESS

2.3 Imaging protocol

We raster-scanned a square field of view (FOV) of 2 × 2 mm^2 using Vis-OCT. For alignment purposes, we acquired low-resolution OCT stacks consisting of 256 × 256 A-lines, which took ~1.3 s to finish. After identifying the desired area of interest, we recorded Vis-OCT angiography data stacks using a uni-directional raster scan with fast fly-back at 400% of the forward speed, recording five repeated B-scan images at the same cross-section before moving to the next. As a result, the entire image stack included 400 × 5 × 512 A-lines, which took ~25.6 s to finish.

We laterally translated the animal holding stage and took multiple Vis-OCT images within each session. These images were later stitched together during post-processing, which provided an extended FOV as large as 3.2 × 3.2 mm^2.

2.4 Vis-OCT angiography

We recovered complex OCT signals following the previously reported FD-OCT reconstruction algorithm [29–31]. The modulus of the complex signal corresponded with the OCT structural images. To generate OCT angiography, we first corrected motion distortions within each group of five repetitive B-scans at the same cross-section. Two algorithms were employed sequentially. First, to correct motion shifts larger than our imaging resolution, we performed image registration using 2D cross-correlation at the pixel level [32]. Each B-scan was then linearly translated back to its zero-shift location. Second, the remaining sub-resolution sub-pixel shifts were corrected using two phase modulators: axial global phase fluctuation (AGFP) and lateral global phase fluctuation (LGFP). Details on the calculation and application of AGFP and LGFP can be found in the references [33].

After motion-shift correction, we calculated the modulus of the complex difference between consecutive B-scans within the same group. Then, the intra-group temporal average was performed to reduce speckle noise. We repeated the process at all 512 B-scan locations to obtain the volumetric OCTA stack. To generate an *en face* angiographic image of the cortical surface, we projected along the axial axis using 15 adjoining pixels with the highest average intensity, which corresponded with the brightest slab approximately 16.2 μm in thickness. The mean axial location of these pixels was further used as the depth coordinate for the corresponding vessel. Pixel remapping and interpolation ensured that the output image had the same aspect ratio as the FOV. Quantitative imaging analysis was then performed using the measurement toolbox in ImageJ.

2.5 Vis-OCT angiography-based oximetry

We calculated cortical blood sO_2 using spectroscopic OCT angiography analysis. To generate wavelength-dependent OCT angiography, we followed the same procedures as described above, except that the raw spectrum was band-selected using the short time Fourier Transform (STFT) technique. Each window was constructed to have an equal width of 0.23 μm^{-1} in k-space, so the spectroscopic OCT angiography image stack will have uniform axial resolution. At 566 nm center wavelength, it corresponded with a spectral bandwidth of 12 nm. We empirically chose the window size to optimize the trade-off between spatial and spectral resolutions. The relaxed axial resolution was about 11.7 μm in air, which was then comparable to the system's lateral resolution.

Without affecting the validity of our spectral analysis, we developed the following formulation based on an ideal OCT system with infinite axial resolution and zero sensitivity roll-off. The modeled wavelength-dependent (λ) depth-resolved (z) angiography intensity (AI) can be related to angiography A-line (AA) using the following model,

$$AI(z,\lambda) = \left[AA(z,\lambda)\right]^2 = I_0(\lambda) r(z,\lambda) \eta(z,\lambda) G(v), \quad (1)$$

Biomedical Optics EXPRESS

where $I_0(\lambda)$ is the incidence light intensity; $r(\lambda)$ is a wavelength-dependent coefficient that characterizes the backward-scattered light that fell within the collection solid angle of the OCT detection; $G(v)$ is a non-negative scalar representing motion contrast enhancements; and v is the local velocity. $G(v)$ is 0 only if the tissue is static. We define $\eta(z,\lambda)$ as the cumulative attenuation when light double-passes the tissue

$$\eta(z,\lambda) = e^{-\int_0^z 2\mu_t(z',\lambda)dz'}, \tag{2}$$

where μ_t is the total attenuation coefficient of local tissue attributed to both optical absorption (μ_a) and scattering (μ_s). As scattering in biological tissue has a strong forward tendency, we estimated μ_t using reduced total attenuation coefficient $\mu_t = \mu_a + (1-g)\mu_s$, where g is the anisotropy factor of the scattering process.

We first used the source spectrum to normalize the detected *AI*. The normalized spectrum I_{norm} encoded optical attenuation from blood, which was then used to calculate sO_2; however, the extracted cortical vessel I_{norm} showed a strong positive correlation against the increasing wavelength, as shown in Fig. 2(a). We believe that such correlation originated from wavelength-dependent back-scattering from cortical tissues, because they are much less transparent compared with retinal tissues. Although our algorithms were developed to correct such a situation, the strong correlation was still detrimental to sO_2 estimations, especially in smaller vessels where SNR was not optimal.

To tackle the problem, we developed a new dual-depth sampling and normalization approach. We implemented threshold-based image segmentation on volumetric OCT angiography stacks to separate vessels from the background. The location of each blood vessel segment in the whole-spectrum OCTA image was then identified and located. We measured wavelength-dependent OCT angiography intensity at two different depth planes for the subsequent spectroscopic analysis. The first measurement was taken near the superficial surface of the vessel (Z_1); the other at a plane 20 – 50 μm beneath the vessel surface (Z_2). The specific depth for Z_2 was determined by the actual vessel diameter so that it always resided within the vessel. Each slab was 10 pixels, or 11.1 μm thick. Thus, the analogous optical density function can be calculated by taking the natural logarithm of the ratio between these two angiography intensities,

$$\begin{aligned} OD &= \ln\left(\frac{AI(z_2,\lambda)}{AI(z_1,\lambda)}\right) = \ln\left(\frac{I_0(\lambda)r(z_2,\lambda)\eta(z_2,\lambda)G(v,z_2)}{I_0(\lambda)r(z_1,\lambda)\eta(z_1,\lambda)G(v,z_1)}\right) \\ &= \ln\left(\frac{\eta(z_2,\lambda)}{\eta(z_1,\lambda)}\right) = -2\bar{\mu}_t(\lambda)d = -2d\left[sO_2\cdot\mu_{HbO_2}(\lambda) + (1-sO_2)\cdot\mu_{Hb}(\lambda)\right], \end{aligned} \tag{3}$$

where $d = z_2 - z_1$. Because both signals originated from the blood, $r(z_2,\lambda)$ equaled $r(z_1,\lambda)$ and they canceled each other in the equation. We carefully tuned the spectrometer integration time and inter-frame dwell time to guarantee that (1) the fringe washout threshold was higher than the peak cortical blood flow rate, and (2) the displacement of blood cells was fully randomized with respect to the illumination wavelength. When both conditions were satisfied, $G(v)$ would lose velocity dependence. Thus, even though blood flow has a parabolic profile within vessels, it had limited effects on $G(\Delta\varphi)$ and the subsequent spectroscopic analysis. Unfortunately, the treatment implied that the blood sO_2 was homogenous within the containing vessel. Although this it is likely to be true in larger pial vessels, smaller

Biomedical Optics EXPRESS

penetrating arteriole and venules may display inhomogeneous sO_2 distribution [34]. Thus, we restrained subsequent quantitative sO_2 analysis on major pial branches, which was also more accessible to visible-light illumination.

For comparison, we plotted $\frac{AI(z_2,\lambda)}{AI(z_1,\lambda)}$, also denoted I_{norm}, from the same artery and vein in Fig. 2(b). The tilt was largely corrected. We also calculated the expected optical attenuation using Beer-Lambert law based on parameters from fully oxygenated and deoxygenated whole blood [dashed lines in Fig. 2(b)] [35]. We can see that the experiment data agrees with the expected theoretical values for wavelengths from 520 nm – 580 nm. The arterial spectrum, due to its high oxygenation, followed the theoretical spectrum of oxygenated whole blood. On the other hand, the venous spectrum showed the combined oxy- and deoxy- whole blood spectrum shape, indicating that it was partially oxygenated. Excessive uncorrected bias also was observed for wavelength outside the range, possibly due to reduced illumination energy and thus low SNR. We excluded these spectral regions in the subsequent analysis. Finally, we performed a non-negative least-square fitting on Eq. (3) to extract sO_2.

To demonstrate that the new approach indeed improved the precision of blood sO_2 measurements, we compared the statistics distribution of their respective sO_2 measurements. Samples were taken from the same pair of artery and vein segment using a 6 × 6 pixel square window (25 × 25 μm^2). We randomly off-set the sampling location within the vessel segment, and a total of 200 samples were taken at each. Then, we applied both our original numerical compensation method and the new dual-depth sampling and normalization approach to calculate blood sO_2. The normalized frequency of calculated sO_2 values were plotted in Fig. 2(c) and (d), respectively. Due to the existence of imaging noise, our original approach tended to underestimate blood sO_2 and had wider distribution range [Fig. 2(c)], leading to a relative large error margin of 89% ± 13% and 72% ± 14% for arterial and venous blood, respectively. On the contrary, our new approach provided more precise and consistent sO_2 estimations, with values of 93% ± 3% for the artery and 75% ± 6% for the vein [Fig. 2(d)].

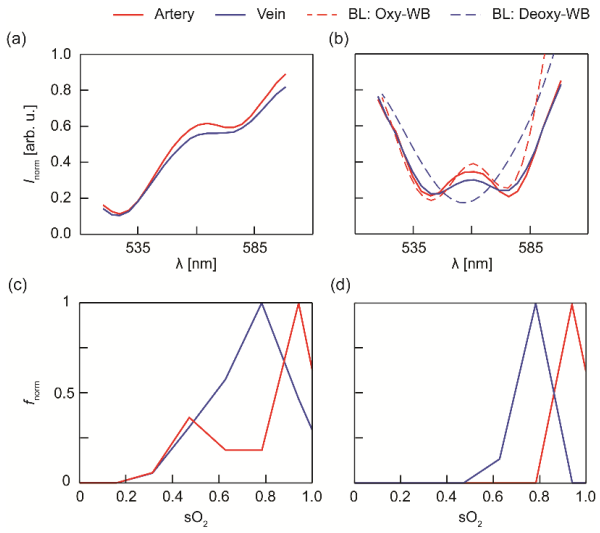

Fig. 2. OCT angiography spectra from selected artery and vein before and after scattering correction. (a) Uncorrected raw OCT intensity spectra. (b) Scattering-corrected OCT intensity spectra. Dashed lines are theoretical intensity spectra for fully oxygenated whole blood (Oxy-WB) and fully deoxygenated whole blood (Deoxy-WB), which are calculated using Beer-Lambert law and compiled literature data for the optical properties of whole blood. (c) Normalized frequency (f_{norm}) of calculated sO_2 using our original method. (d) f_{norm} of calculated sO_2 using the new dual-depth sampling and normalization method.

Biomedical Optics EXPRESS

3. Results

3.1 Vis-OCT angiography

Figure 3 compares the depth-encoded OCT angiographs before and after photothrombosis. The ischemic core can be identified, as the OCT angiography intensity within the region fell below our detection sensitivity due to the lack of flow-enhanced motion contrast [Fig. 3(b)]. In addition, we observed a similar vascular network over the non-occluded region in both *en face* projections. Most major vessels, e.g., middle cerebral artery (MCA, denoted A) and superficial pial veins (denoted V), resided close to the cortex surface, typically within 50 μm below the surface. In contrast, smaller vessel branches and capillary bed dived deeper into the cortical tissue, reaching a depth of 85 μm and beyond. These findings agreed with the physiological arrangements of mouse cerebral circulation reported in earlier publications [13]. In addition, we observed some minor lateral and depth variations in the vessel location between the two images. We believe the slight shift was caused by a certain degree of edema and fluid accumulation that developed after vessel occlusion [25]. Direct comparison of two angiographic B-scans from two different locations, as indicated by dashed lines, showed diminished OCTA intensity within the occluded region [Fig. 3(c) and (d)].

Biomedical Optics EXPRESS

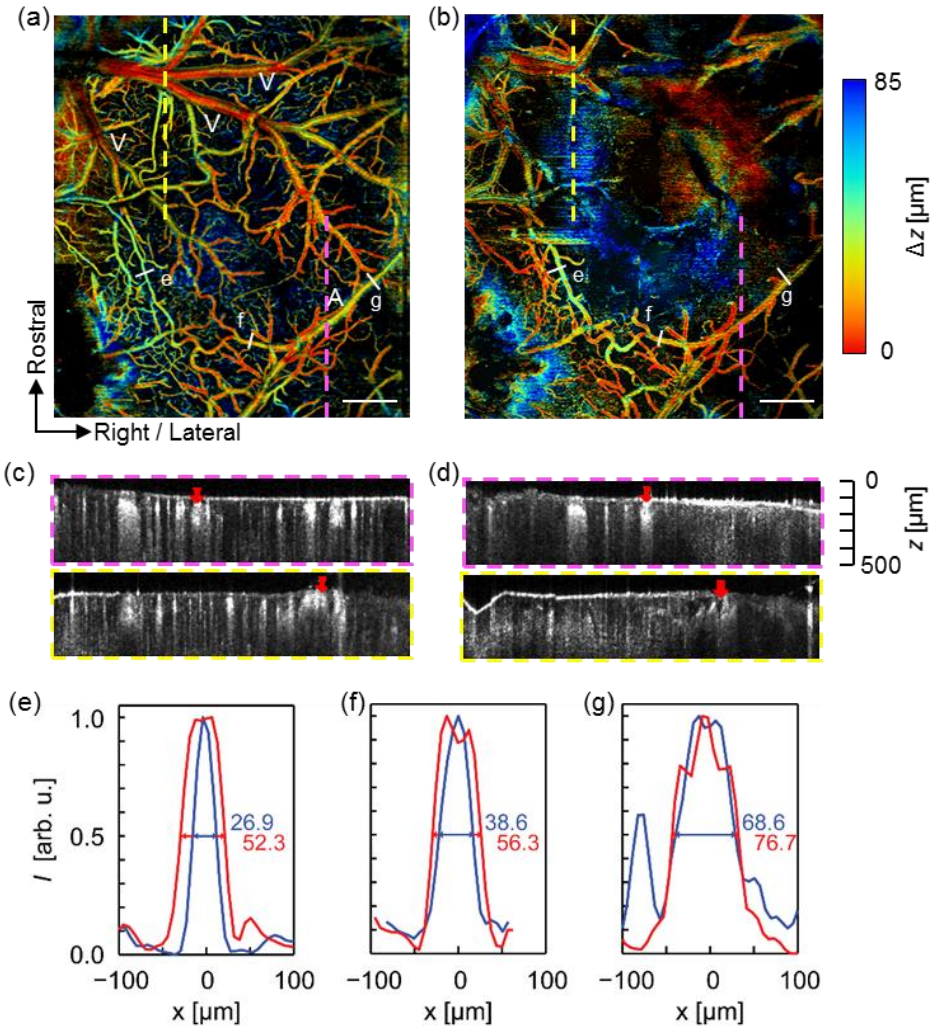

Fig. 3. Depth-coded OCT angiograph in a mouse cortex before and after focal ischemic stroke. (a) Pre-photothrombosis microvascular structure. A: middle cerebral artery. V: superficial pial veins (b) Post-photothrombosis microvascular structure. Scale bar: 500 μm. (c) and (d): OCT B-scan images taken from respective locations indicated by colored dashed line in (a) and (b). The red arrows indicate main artery (in purple square) and vein (in yellow square), respectively. (e)-(g) Vessel profile taken from respective lines indicated in (a) and (b) showing vessel dilation after photothrombosis. Blue line: pre-photothrombosis; red line: post-photothrombosis.

The post-photothrombosis OCT angiography revealed universal vessel dilation across the non-occluded area within the FOV. We measured the vessel profiles and FWHM diameters at the locations indicated by labels (e), (f), and (g). These vessels have different sizes, and (f) and (g) were identified by experts to belong to different branches of the middle cerebral artery. For each of these vessel segments, the observed vasodilation was 94.4%, 45.9%, and 11.8%, respectively, where smaller vessels tended to have a larger percentage of increase in diameter. The observation agreed with previous reports on mouse cortex using the transient middle cerebral artery occlusion (tMCAO) model [36]. It was hypothesized that active vessel regulation in response to regional hypoxia challenge may have played a major role in mediating vessel dilations. In addition, Ishikawa et al. conducted photothrombotic experiments on rat cortex and reported similar observations [37]. In the same study, Ishikawa

Biomedical Optics EXPRESS

et al. proposed that free radial activation, i.e., hydroxyl radicals, served as a potential vasodilator following focal photothrombosis. Nevertheless, our experimental results agreed with the widely held knowledge that extensive vascular remodeling and blood flow redistribution are expected following cortical vessel occlusion.

3.2 Vis-OCT angiography-based oximetry in brain cortex

Using the algorithm previously described, we retrieved the spectroscopic OCT angiography spectrum and calculated absolute sO_2 pixel-by-pixel within each identifiable vessel. Then, we smoothed the resulting sO_2 maps using a Gaussian window about the size of system lateral resolution (12 μm). Figure 4 shows the two cortical oxygenation maps before and after photothrombosis. In the pre-photothrombosis image [Pre-PT, Fig. 4(a)], arteries and veins could be identified according to their measured sO_2 values in pseudocolors. The identification agrees with our previous classification based on the orientation and morphology of the cortical vessels; however, we also noticed that only averaged sO_2 can be measured in the regions where the artery and vein overlapped with each other. One of such regions was highlighted in the elliptic circle in Fig. 4(a); in contrast, such differentiation was no longer observable in the post-photothrombosis image [Post-PT, Fig. 4(b)].

We further extracted the mean sO_2 value along different branches of vessels. We found that sO_2 within the arteries decreased as oxygen unloaded into the tissue. For example, in the first imaged branch of the middle cerebral artery (A_1), the measured sO_2 value was 93 ± 3%. The value agreed with systemic oxygen saturation (spO_2) of 95%, as measured by the pulse oximeter. The mean sO_2 dropped to 90 ± 3% as it traveled and oxygen unloaded into regional tissue in the next branch (A_2). We also observed a similar trend in veins: we identified three consecutive branches of an identified vein (V_1 to V_3), with V_1 as the largest and V_3 the smallest. After calculation, we found that V_3 had the lowest sO_2 at 73 ± 4%, while V_1 had the highest at 86 ± 8%. The mean sO_2 from the V_2 branch fell in between (i.e., 80 ± 4%). In the post-photothrombosis image [Fig. 4(b)] such difference disappeared. The vessels had a uniform green-blue color, indicating a mean sO_2 below 70%. The same vessel branches labeled as A_1 and A_2 had a mean sO_2 value 67 ± 7% and 64 ± 6%, respectively [Fig. 4(c)].

Biomedical Optics EXPRESS

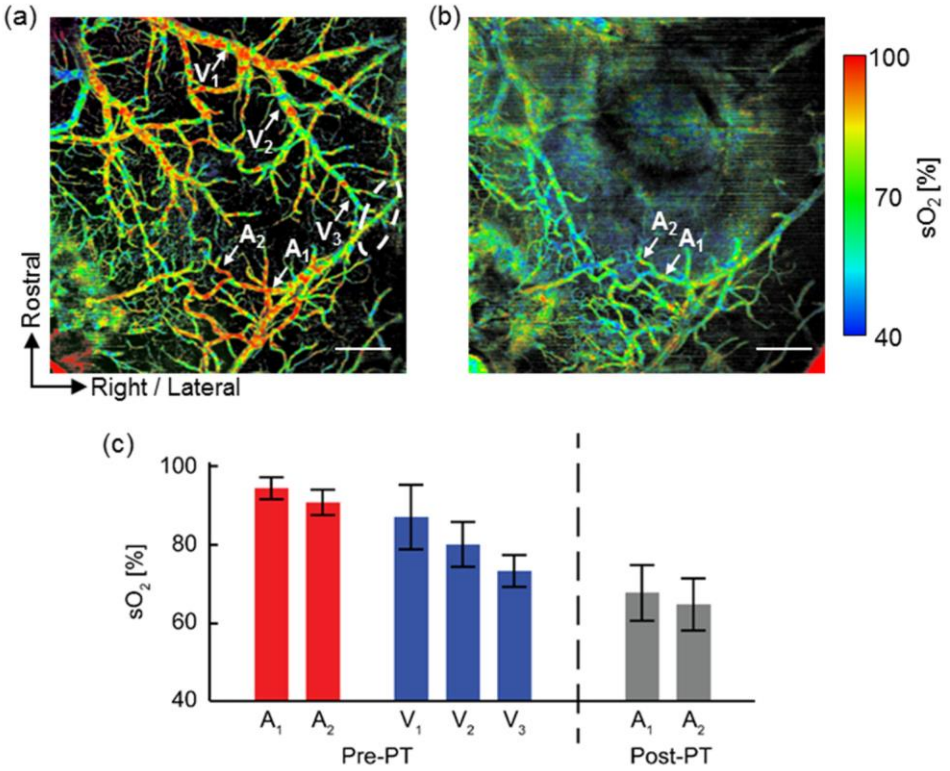

Fig. 4. Vis-OCT angiography sO_2 map before and after focal ischemic stroke. (a) Before photothrombosis (Pre-PT). (b) After photothrombosis (Post-PT). Scale bar: 500 µm. Arrows indicate the vessels where mean sO_2 was calculated. Elliptical area indicates where arteries and veins overlapped each other and the averaged sO_2 was displayed. (c) Mean sO_2 values from the selected vessels. A1-A2: first- and second-order branches of middle cerebral artery. V1-V3: first-, second-, and third-order branches of a vein. Error bar: S.D.

4. Discussion and conclusion

In the presented work, we demonstrated that Vis-OCT angiography can be used to monitor hemodynamic variations in the cortical circulation in mouse. We developed a novel sampling and normalization approach that sampled two OCT angiography intensity at different depths within the blood vessel. Using OCT angiography rather than a structure OCT signal, we simplified the required image segmentation algorithm, and, more importantly, enhanced the visibility of smaller vessel branches that are otherwise invisible. The generated full-field sO_2 map revealed oxygen unloading within arterial vessels. We also observed that pial venular sO_2 increases with vessel diameter. Similar observations were previously reported on mouse cortex using function two-photon microscopy [34], as well as in different organs [38]. Two hypotheses have been proposed [34]: (1) Arteriovenous communication pathways allow direct oxygen advection, thereby elevating venous sO_2 in larger pial branches. Though scarcely reported, such communicating pathways may exist [39]. (2) oxygen can diffuse back toward venules where tissue oxygen partial pressure is higher [40]; however, due to the complex and heterogeneous nature of the cerebral microvascular network, we cannot identify the exact explanation without further investigation.

Although, theoretically, we can use the axial information provided by the volumetric OCT angiography stack to calculate the absolute concentration of oxyhemoglobin (HbO) and deoxyhemoglobin (HbR), we opted to calculate only the relative HbO_2 and HbR

Biomedical Optics EXPRESS

concentration, $sO_2 = \frac{[HbO_2]}{[HbO_2]+[HbR]}$, due to following considerations. First, calculating absolute hemoglobin requires knowing the path length parameter *d*; however, the employment of STFT comprised our axial resolution to around 12 μm. Given that the depth separation between two sampling locations could be as small as 20 μm in smaller vessels, we could generate a large error margin when using such inaccurate estimations. Second, total hemoglobin concentration is unlikely to change significantly during the short imaging period, while its value can be conveniently and accurately measured from blood samples using well-established methods. In contrast, measuring local sO_2 was much more challenging and it revealed more crucial information on oxygen metabolism than absolute hemoglobin concentrations.

We were aware that Rose Bengal (RB) dye had an absorption spectrum similar to that of HbR in the wavelength range we used [Fig. 5(a) in the Appendix]. If excessive RB was present in the circulation system, it would have led to sO_2 underestimation. Fortunately, RB has high blood clearance rate: its initial plasma half-life was previously characterized to be around 2 minutes at low blood concentrations [41]. At the dosage used, the RB blood concentration would fall below our detection limit at the end of 30 minutes exposure time; therefore, it was unlikely that the use of RB would have a significant impact on the reported sO_2 values.

To verify our hypothesis, we performed a controlled experiment measuring blood RB clearance in mouse using quantitative fluorescent microscopy. The RB plasma concentration was monitored at 8, 16, 24, and 32 minutes post-tail vein injection. Only trace amount ([RB] = 0.019 mM, versus [HbT] = 2.3 mM) of RB was detected after the 24-minute mark [Fig. 5(b),5(c)]. The results indicated that blood RB concentration was extremely low when we took Vis-OCT measurements, and that our sO_2 measurements were valid; however, if continuous monitoring during the entire focal ischemia is desirable, high plasma RB surely will introduce sO_2 underestimation. Therefore, photothrombois is not the preferred model if blood sO_2 is to be optically determined on a continuous basis and thus other surgically induced models should be used.

One drawback of the presented approach is that it was unable to retrieve useable angiography data within the ischemic core. Fortunately, this implication will depend on the specific aims of different studies. In most cases, neurons in the region will inevitably undergo cell death due to severe oxygen deprivation; therefore, such measurements offer limited insight because there are no surviving cells. In contrast, the Vis-OCT angiography approach successfully retrieved hemodynamic parameters in the penumbra region, which was the primary target in most stroke studies. Nevertheless, we agree that the non-blood-flow-based method, e.g., regular structure OCT oximetry, functional two-photon fluorescence microscopy, photoacoustic microscopy, and functional magnetic resonance imaging, can be more desirable if the oxygen metabolism around the ischemic core needs to be measured.

In summary, our Vis-OCT angiography and oximetry provided quantitative tools for analyzing hemodynamic response in mouse cortex. Although only demonstrated on a mouse ischemic stroke in the presented study, these tools potentially have much broader applications, such as in cancer angiogenesis and traumatic brain injury studies, where the quantification of cortical hemodynamic response is required.

Biomedical Optics EXPRESS

Appendix

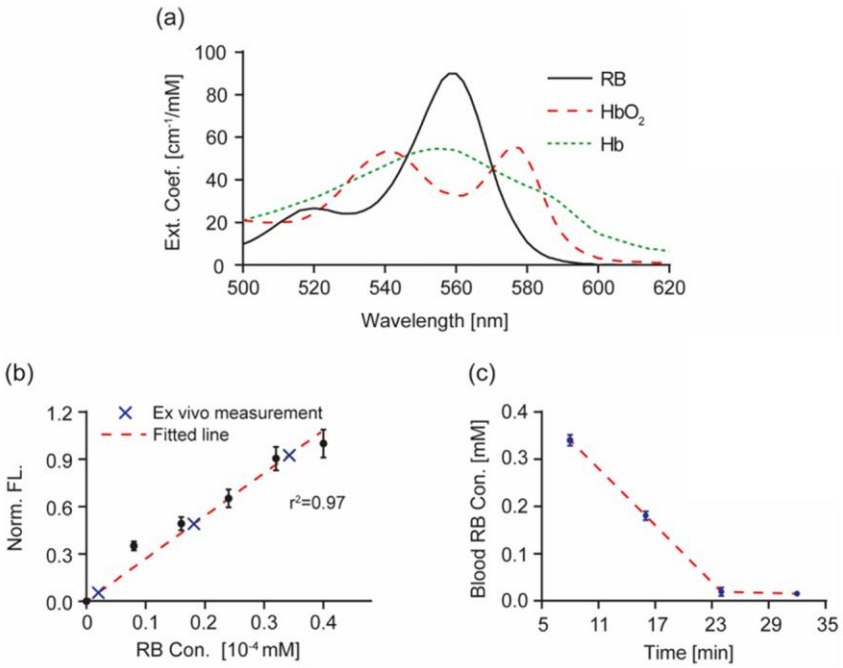

Fig. 5. Measurement of mouse blood Rose Bengal (RB) concentration using quantitative fluorescence (FL) analysis. (a) Extinction spectra of RB, oxy-hemoglobin (HbO_2) and deoxy-hemoglobin (Hb). These three chromophores have overlapping strong absorption within the wavelength range from 500 nm – 620 nm. (b) Calibration curve for quantitative FL measurement of RB concentration. Normalized FL intensity from RB solution is plotted against its known concentrations (black dots, error bar: S.D.). FL intensity showed strong positive correlation with RB concentration. We performed linear regression to retrieve the calibration curve (red dashed line, $r^2 = 0.97$). (c) Blood RB concentration as estimated using quantitative FL measurements at time points 8, 16, 24, and 32 minutes after intravenous RB injection. Blood samples were diluted 10,000 times prior to FL measurement to prevent fluorescence quenching and virtually eliminated blood optical absorption. The first three measurement points are plotted onto the calibration curve in (b) (blue crosses), then converted to blood RB concentration and plotted against time in (c).

Funding

National Institute of Health (NIH) (1R24EY022883, 1DP3DK108248); National Science Foundation (NSF) (CBET-1055379, DBI-1353952); Natural Science Foundation of China (NSFC-61371018); and China Scholarship Council (201406230188).